Research Article Vol. 59, No. 30 / 20 October 2020 / Applied Optics 9499

applied optics

Role of scattering by surface roughness in the photoacoustic detection of hidden micro-structures

Vanessa Verrina,[1,2,*] Stephen Edward,[1,2] Hao Zhang,[1,3] Alessandro Antoncecchi,[1,3] Stefan Witte,[1,3] and Paul Planken[1,2,4]

[1]Advanced Research Centre for Nanolithography (ARCNL), Science Park 106, 1098 XG Amsterdam, The Netherlands
[2]Van der Waals-Zeeman Institute, University of Amsterdam, Science Park 904, 1098 XH Amsterdam, The Netherlands
[3]Department of Physics and Astronomy, Vrije Universiteit, De Boelelaan 1081, 1081 HV Amsterdam, The Netherlands
[4]e-mail: p.planken@arcnl.nl
*Corresponding author: v.verrina@arcnl.nl

Received 8 May 2020; revised 18 September 2020; accepted 18 September 2020; posted 21 September 2020 (Doc. ID 397264); published 19 October 2020

We present an experimental study in which we compare two different pump–probe setups to generate and detect high-frequency laser-induced ultrasound for the detection of gratings buried underneath optically opaque metal layers. One system is built around a high-fluence, low-repetition-rate femtosecond laser (1 kHz) and the other around a low-fluence, high-repetition-rate femtosecond laser (5.1 MHz). We find that the signal diffracted by the acoustic replica of the grating as a function of pump–probe time delay is very different for the two setups used. We attribute this difference to the presence of a constant background field due to optical scattering by interface roughness. In the low-fluence setup, the optical field diffracted by the acoustic replica is significantly weaker than the background optical field, with which it can destructively or constructively interfere. For the right phase difference between the optical fields, this can lead to a significant "amplification" of the weak field diffracted off the grating-shaped acoustic waves. For the high-fluence system, the situation is reversed because the field diffracted off the acoustic-wave-induced grating is significantly larger than the background optical field. Our measurements show that optical scattering by interface roughness must be taken into account to properly explain experiments on laser-induced ultrasound performed with high-repetition-rate laser systems and can be used to enhance signal strength.

https://doi.org/10.1364/AO.397264

1. INTRODUCTION

Positioning of silicon wafers with (sub)nanometer precision during photolithography is one of the biggest challenges in the semiconductor manufacturing industry [1–5]. In photolithographic machines, alignment markers etched into Si wafers are used to position wafers with sub-nanometer accuracy. These markers are often gratings illuminated with lasers, while the diffracted beams are measured. Any difference in optical phase between the +nth and −nth diffracted orders (n = 1, 2, 3 …) can be measured by interfering the two beams. A small translation of the wafer along the grating vector direction translates into a phase difference between the +nth and −nth diffracted orders, which can be used to determine the position of the wafer with a precision of less than 1 nm [4,5]. Alignment becomes challenging when (partially) opaque materials are used to fabricate computer chips with multilayer architectures, so that light cannot penetrate them anymore, and the alignment markers become difficult to probe. In reality, alignment gratings are etched in areas where there are no circuits, in the so-called scribe lanes. Nevertheless, they get covered by all the materials used in the fabrication processes of the computer chips. Hence, methods need to be developed that are capable of detecting micro- and nano-structures buried below layers that may even be optically opaque. In addition, measurement methods should remain non-invasive, in the sense that they should not damage or even touch the sample or otherwise influence subsequent lithographic processing steps.

An alternative way to detect gratings buried underneath optically opaque layers is therefore to use laser-induced ultrasound. It is based on the absorption of a picosecond or femtosecond laser pulse, which leads to the creation of acoustic waves in the tens of gigahertz range [6–26]. Fundamentals of laser-induced acoustic waves have been studied extensively in the past decades [6–9]. The ability of acoustic waves to propagate through layers

that are not transparent to light has led to many applications, such as high-resolution photoacoustic imaging [19–22] and material characterization, providing information on layer thickness, sound velocity, and interface properties [14–16,27–30]. Moreover, spatial inhomogeneity of the illuminated surface can lead to excitation of shear waves and surface acoustic waves (SAWs) [10–12].

We recently showed that laser-induced ultrasound can be employed for the detection of micro- and nano-structures buried underneath metal layers [31]. With this technique, we were able to detect gratings underneath optically opaque layers and dielectric multilayers, even after propagation of the acoustic wave through as many as 2×20 dielectric layers. The buried grating was observed by measuring optical diffraction from the acoustic replica of the grating at/near the interface/surface in a pump–probe scheme. As the amplitudes of the acoustic-wave-induced gratings are in the 1–100 pm range, diffracted signals can be small. As a result, other weak sources of scattered or diffracted signals can lead to interference with the light diffracted by acoustic-wave-induced gratings. Understanding these effects is of paramount importance for possible wafer alignment applications in the semiconductor manufacturing industry. This is because positioning errors of only a few nanometers, potentially the results of a wrong interpretation of photoacoustic diffraction signals, would already be disastrous.

Here, we show how light scattered by interface/surface roughness can influence the shape and amplitude of the time dependent diffracted signal in ultrafast photoacoustics experiments to detect micro-gratings buried underneath opaque layers. As we found that the pump–pulse fluence is an important parameter in our experiments, we used two different lasers with accompanying setups, one for low-fluence experiments (LFEs), the other for high-fluence experiments (HFEs). For our experiments, 6 μm period, 50% duty cycle gold (Au) gratings were fabricated on top of a single metal layer deposited on glass. A 400 nm wavelength pump pulse generates ultrahigh-frequency longitudinal acoustic waves near the glass–metal interface, which travel deeper into the Au and reflect off the grating. The topography of the grating is thus encoded on the phase of the acoustic wave and detected at the glass–metal interface by diffraction of an 800 nm wavelength probe pulse. Surprisingly, we find that the signals measured in the two setups look very different, even though experiments were performed on the same sample. For example, despite the fact that in both cases, the timing of the acoustic peaks is more or less the same, the signals measured in the HFE are all positive, while the signals measured in the LFE periodically drop below the background level. We show that these and other observations can be explained by the presence of a coherent optical field caused by scattering due to interface roughness, which interferes with the optical field diffracted off the acoustic-wave-induced gratings. For the right optical phase difference, the relatively strong background field can enhance (coherently amplify) the weak field diffracted by the acoustic-wave-induced grating. Our experiments are in excellent agreement with numerical simulations that can predict the exact shape of the signals measured in both HFEs and LFEs. Our results show the importance of interface/surface roughness in understanding the results obtained using a low-fluence, high-repetition-rate femtosecond laser for ultrafast photoacoustic detection of nano-structures buried below optically opaque layers.

2. SAMPLE FABRICATION AND OPTICAL SETUPS

Samples were made by first depositing a flat metallic layer on a glass substrate, followed by fabrication of a grating on top of the metallic layer. By performing the pump–probe measurement from the glass side, the grating is optically invisible to both the pump and probe pulses and can be considered "buried." This can be seen in the inset of Fig. 1. All the samples were made on chemically cleaned 176 μm thick glass substrates. The Au layers were deposited by thermal evaporation. All gratings employed in the experiments were fabricated using UV lithography. Each grating has a period of 6 μm, a 50% duty cycle, and an amplitude of 10 nm. The three samples employed in this work differ only in the thickness of the flat Au layer, (85, 141, and 522 nm).

Our experiments were performed in a pump–probe setup, shown in Fig. 1. Two different setups were used. The first is built around a low-fluence Ti:sapphire laser that generates 70 fs pulses at a high repetition rate of 5.1 MHz. Here, the pump beam has a diameter of 50 μm on the sample and a pulse energy ranging from 8 nJ to 15 nJ, depending on the experiment. The probe has a diameter of 40 μm on the sample, and its pulse energy is kept constant at approximately 12 nJ. The pulse energies generated by this system are relatively low, and we will refer to experiments performed with this laser as LFEs.

The second is built around a high-fluence, amplified Ti:sapphire laser that generates 30 fs pulses at a low repetition rate of 1 kHz. Here, the pump diameter is approximately 500 μm, and pump pulse energies range from 6 μJ to 8 μJ, depending on the sample. The probe has a diameter of 250 μm on the sample, and the probe pulse energy is kept constant at 2 μJ. The pulse energies generated by this system are higher, and we will refer to experiments performed with this laser as HFEs.

In both setups, the 800 nm wavelength output is split into two parts. The stronger arm is frequency doubled to generate 400 nm wavelength pulses and is used as the pump beam. The weaker arm is time delayed using an optical delay line formed by a retroreflecting pair of mirrors mounted on a mechanical translation stage and is used as the probe beam.

We would like to point out that in wafer alignment applications, the pump fluence is often maximized to values just below the damage threshold to maximize the strength of the diffraction signal. In principle, both high and low fluences can be obtained with one laser, by simply changing the focal diameter of the beam. However, there are two reasons that we nonetheless have used two different laser systems in these experiments. The first is that the highest fluence that we can obtain with the low-fluence, high-repetition-rate system is limited by thermal damage, preventing us from reaching the fluence levels reached in the HFE. The second is that, whereas it is tempting to think that the HFE is better than the LFE because it can generate stronger acoustic waves, the sensitivity with which these waves can be detected is limited compared to what is possible in the LFE. The reason for this is that in the LFE, the much higher repetition rate of the laser (5.1 MHz) allows for laser amplitude modulation at frequencies (we use 6 kHz) where lock-in amplification of

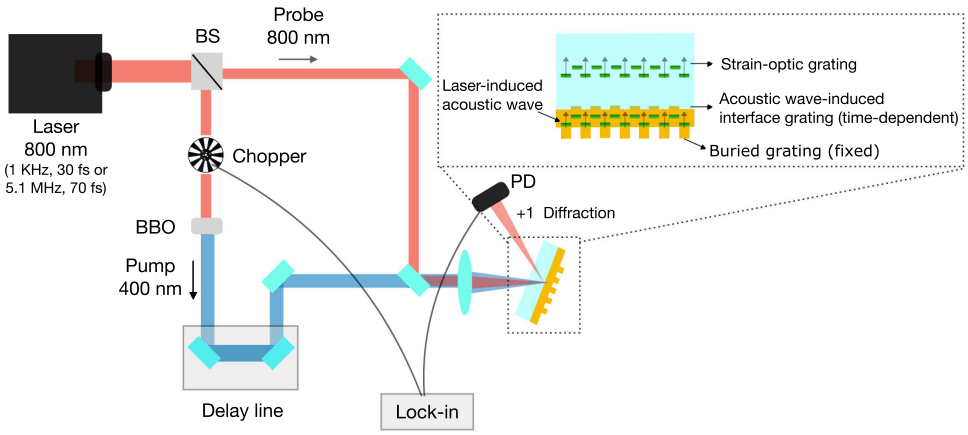

Fig. 1. Schematic of the two experimental setups. In both setups, a pump–probe scheme was employed. The output from a 1 kHz or 5.1 MHz repetition rate Ti:sapphire laser with a central wavelength of 800 nm is split into two parts. One beam (pump) is frequency doubled to a wavelength of 400 nm by a BBO crystal and modulated by a mechanical chopper at 6 kHz. The other beam (probe) has a central wavelength of 800 nm. The pump-induced first-order diffracted probe beam is measured by a silicon photodiode. The photodiode has a bandwidth of 50 kHz. For the LFE, the photodiode signal is sent to a lock-in amplifier, which uses a reference signal from the chopper. We show in the inset a schematic of the sample. We pump and probe from the glass side. Thus, the measured total diffracted signal is due to diffraction off the interface grating and off the strain-optic gratings in glass.

the electronic signal from the photodiode detector can significantly enhance the detection sensitivity. In the end, for wafer alignment applications in the semiconductor manufacturing industry, sensitivity is of paramount importance. However, even without additional contributions to the detected light, such as light scattering by surface roughness, it would be nontrivial to predict *a priori* which system is best for alignment applications. As we will show, light scattering by surface roughness can occur; it interferes with the light diffracted by acoustic-wave-induced gratings, and the extent to which it thus influences the time-dependent shape of the photoacoustic signals depends on the pump fluence.

Finally, we note that in both HFEs and LFEs, it is expected that the frequency of the generated sound waves depends on neither the fluence nor the repetition rate of the laser. The shape and thus the frequency contents of the sound wave are determined primarily by the diffusion depth of the electron energy, which is the same for both LFEs and HFEs.

3. EXPERIMENTAL RESULTS

In Figs. 2(a) and 2(b) (green curves, top panels), we plot the diffracted probe beam signal as a function of the pump–probe delay, measured for the Au grating fabricated on an 85 nm thick Au layer for the LFE and HFE, respectively. In both setups, the signal is first composed of a sharp peak at zero delay. This peak is the result of a grating in the electron temperature near the glass–Au interface, which leads to diffraction of the probe beam and has been measured before [32]. A few tens of picoseconds later, an oscillatory signal with a period of 50 ± 2 ps is observed. The oscillation appears to last several hundreds of picoseconds for the measurements performed with the LFE [green curve in Fig. 2(a)] measurement, while it decays faster for the HFE [green curve in Fig. 2(b)]. A first observation is that the signal shapes measured in the two setups are remarkably different in spite of the fact that both signals were obtained by measuring on the same sample. In particular, we observe "negative" values for the diffracted signal measured in the LFE.

In Figs. 2(c) and 2(d) (green curves, top panels), we show the measurements for the 50% duty-cycle grating fabricated on a 141 nm thick Au layer. As before, a small hot electron dynamics peak at zero time delay is observed. Here, the strength of the electron dynamics signal is smaller than for the grating fabricated on an 85 nm Au layer, since the electron gas temperature grating is weaker for thicker Au layers [32]. A few tens of picoseconds later, an oscillatory signal with a period of 80 ± 2 ps is seen. Compared to the previous measurements, the oscillation appears to decay faster in both the LFE and HFE. Here, too, we observe "negative" values for the diffracted signal for the LFE [green curve in Fig. 2(c)].

In Figs. 2(e) and 2(f) (green curves, top panels), we show the measurements for the 50% duty-cycle grating fabricated on a 522 nm thick Au layer. Here, the electronic peak around delay zero is not detected. For the first 170 ps, no diffracted signal is observed. After this, a diffracted signal can be seen, which rises to a maximum at a delay of 285 ± 2 ps. A second peak is seen around 570 ± 2 ps time delay. A faster oscillating signal is superimposed on top of the acoustic echoes with a period of about 50 ± 2 ps. As before, we observe "negative" values for the diffracted signal for the LFE [green curve in Fig. 2(e)].

A somewhat unexpected observation we made during the experiments in the LFE on the 522 nm Au sample is that the amplitude of the measured signal varies when measuring on different spots on the same sample. Moreover, the signal can even change sign, as if multiplied by ≈ -1. We will explain this in more detail in Section 5. This behavior is absent for the measurements taken in the HFE, where intensity variations were seen of only 10%–20%.

In a series of measurements, we recorded the diffracted signal at different positions above the buried grating fabricated on the 522 nm thick Au layer. The thickest sample was chosen here to

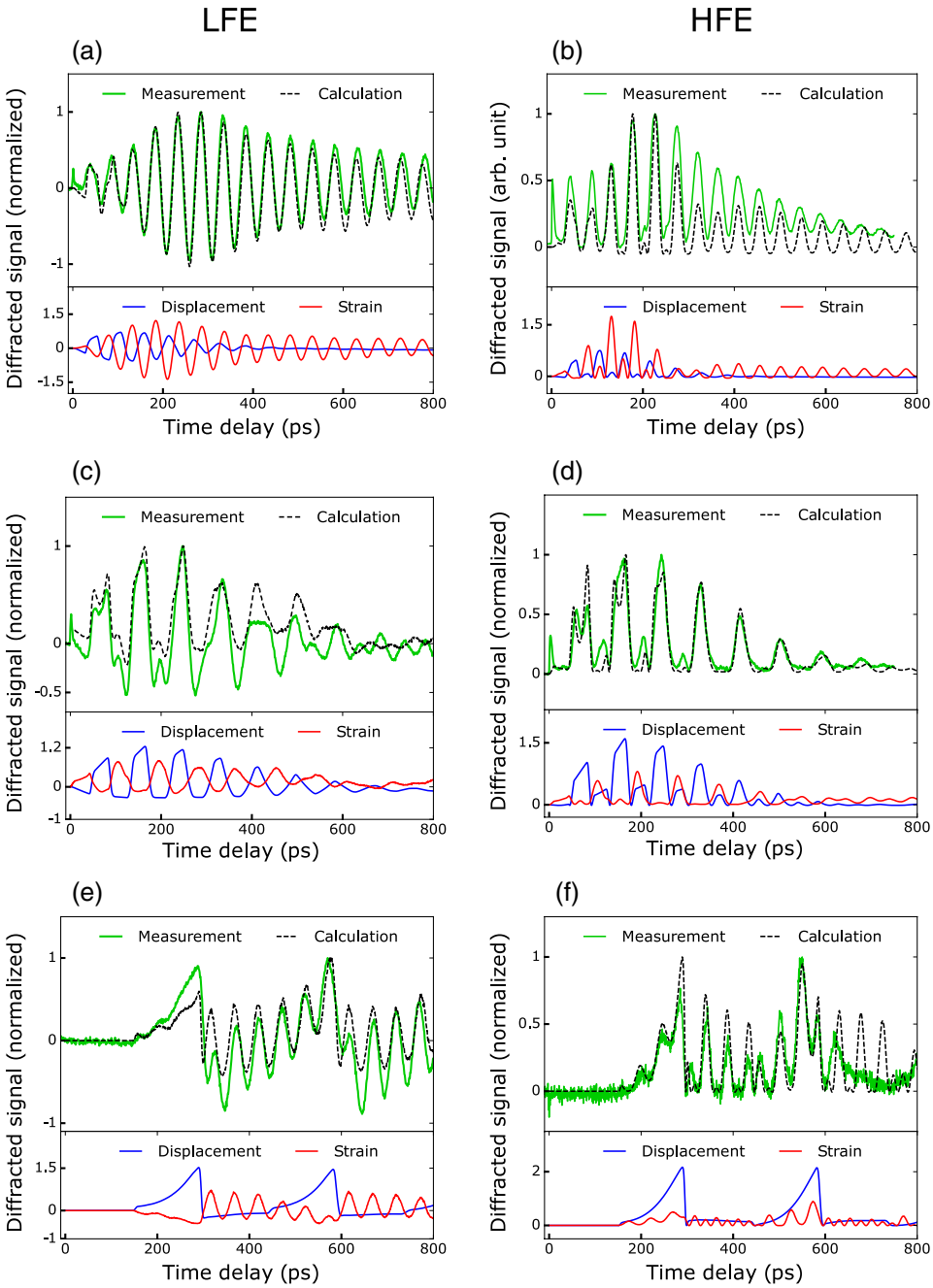

Fig. 2. Diffracted probe beam signal measured for the 50% duty-cycle, 10 nm amplitude Au gratings in the LFE (left) and HFE (right). Top panels: experimental results (green curves) and calculated total signal (dashed black curves). Bottom panels: numerical calculations of the diffracted signals taking into account *only* surface displacement at the glass–Au interface (blue curves) or *only* diffraction from the acoustic waves in glass (red curves). We show the results for: Au grating fabricated on a 85 nm Au layer measured in the (a) LFE and (b) HFE; Au grating fabricated on a 141 nm Au layer measured in the (c) LFE and (d) HFE; Au grating fabricated on a 522 nm Au layer measured in the (e) LFE and (f) HFE.

avoid any effects that could arise from direct optical diffraction from the buried grating. Taking the 13 nm penetration depth of the 800 nm light into account, and in view of the small signals that we measure, this cannot *a priori* be excluded for the thinnest 85 nm thick sample. We first measure the diffracted signal on one particular spot, which we consider the "zero position" (x_0) [Fig. 3(a), top panel]. When the sample is horizontally translated, in the direction perpendicular to the grating's lines, by 50 μm [Fig. 3(a), bottom panel], corresponding to the diameter of the probe beam, or more, the measured signal can change sign compared to the measurement at the previous position. A similar observation is made when we move the sample 50 μm in the vertical direction, parallel to the grating lines, as shown in Fig. 3(b). We note, however, that the signals plotted in Figs. 3(a) and 3(b) were chosen precisely because in these cases, when the sample was moved, the signals flipped sign. To investigate

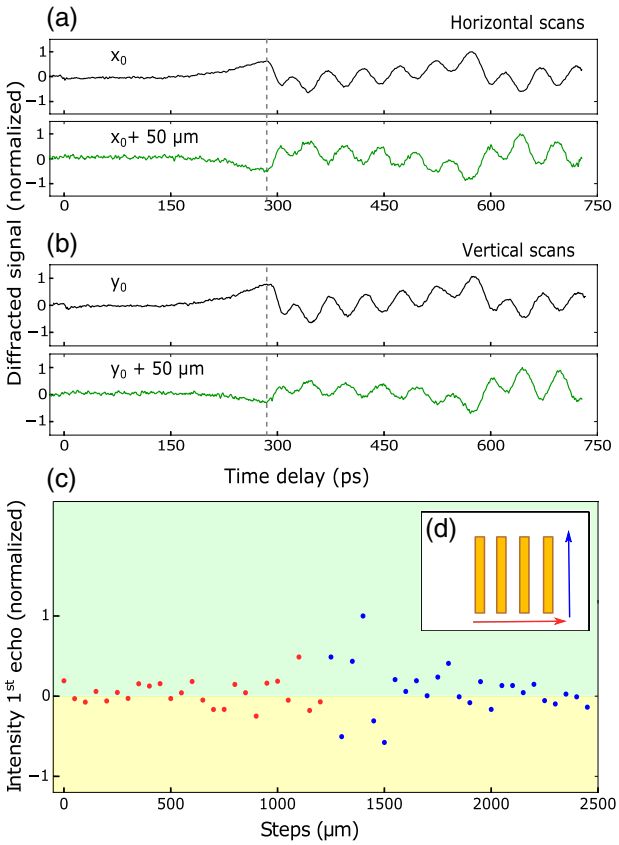

Fig. 3. Diffracted signal recorded at different positions above the buried grating fabricated on the 522 nm thick Au layer. (a) Two extreme cases, where a flip in sign is observed during the horizontal scan of the sample; (b) same for the vertical scan. (c) Intensity of the first echo (corresponding to a time delay of 285 ps) as a function of the position on the sample. The red dots represent the horizontal scan and the blue dots the vertical scan. The yellow area contains the negative values, while the green one contains the positive values. (d) Inset: path followed during the scan schematically shown with the colored arrows.

whether these changes were random or not, we also performed a scan of the sample by recording the diffracted signal while moving the sample in steps of 50 µm, in both horizontal and vertical directions. In Fig. 3(c), we plot the strength of the first diffraction peak (corresponding to a time delay of 285 ps) as a function of the position on the sample. The red dots represent the horizontal scan, where the first data point corresponds to the "zero position" (x_0). The blue dots represent the vertical scan, where the first data point corresponds to the position y_0. The path followed during the scan is shown with the colored arrows in the inset [Fig. 3(d)]. We can clearly see from this plot that the sign and amplitude of the signal seem to vary quite randomly.

When scanning in the area corresponding to the intersection between the horizontal and vertical scans, a stronger variation in the intensity of the diffracted signal is detected. This increase is most likely due to the presence of dust particles trapped between the Au layer and the glass substrate, as observed with a microscope camera. The dust particles give rise to an increased amount of scattered light [33]. As we will discuss later, the results

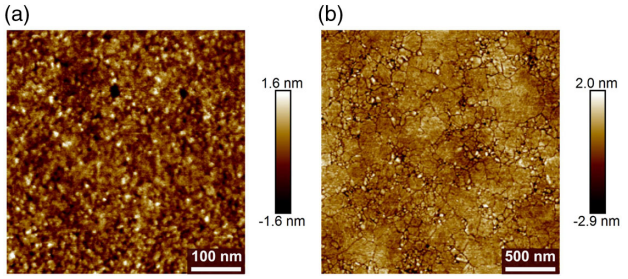

Fig. 4. (a) AFM measurement on the glass side of the glass–Au interface. The roughness is 0.45 nm (RMS value). (b) AFM measurement on the Au side of the glass–Au interface. The roughness is 0.60 nm (RMS value). When deposited on a smooth substrate, the Au tends to follow the topography of the substrate. Therefore, the measured roughness values for glass and Au are in reasonable agreement.

for the LFE can be explained only by taking the optical interference among the field diffracted by the acoustic-wave-induced interface grating, the strain-optic grating propagating in glass, and an *additional* background field into account. The most likely source of this field is optical scattering by the roughness of the metal film at the glass–Au interface.

Scattering from surfaces with a root-mean-square (RMS) roughness amplitude in the range of a few nanometers was measured before [34]. In order to measure the roughness of the Au layer at the glass–metal interface, the Au layer was peeled from the glass substrate by using standard tape in order to obtain a *free-standing* Au surface. In this way, we were able to measure roughness on both the Au side and the glass side of the interface. It is well known that thin Au films have a weak adhesion to inert and commonly used glass substrates [35]. Therefore, by applying a piece of tape onto the sample, it was easy to completely peel the Au layer from the substrate. An atomic force microscopy (AFM) measurement of this layer was then performed. For comparison, an AFM measurement was also performed on the glass surface. In Figs. 4(a) and 4(b), we show the AFM results for the two surfaces. We measure a RMS roughness value, R_q, with values of $R_q = 0.60$ nm for Au and of $R_q = 0.45$ nm for the glass substrate. The two values are in reasonable agreement. Basically, the roughness of the substrate translates into a similar roughness for the deposited metal layer, although the two surfaces look different. In fact, the evaporated Au has a polycrystalline nature, while the glass is an amorphous material. The RMS amplitude roughness of the interface is small and thus gives rise to a weak background field only. However, the amplitude of this field is within an order of magnitude of the amplitude of the field diffracted by the acoustic-wave-induced grating, as we will show later. This means that interference between the two fields can have a significant effect on the amplitude and shape of the time-dependent diffraction signals.

4. RESULTS OF NUMERICAL CALCULATIONS

To better understand our measurements, numerical calculations were performed. The 2D numerical model we used was developed by Zhang *et al.* [36]. It takes into account all the steps involved in a typical photoacoustic experiment, such as

generation, propagation, and detection of the acoustic waves. As for the detection part, diffraction of light off the acoustic-wave-induced interface grating at the glass–metal interface, and off the acoustic grating propagating inside the glass (strain-optic scattering [37]) were both taken into account. In a separate photoacoustic experiment on simple, flat Au layers, material parameters were extracted by fitting the model to the measurements. The same parameter values were then used to fit the model to the measurements shown in Fig. 2. The fitting procedure used to extract the material parameters for the single flat Au layers is extensively described in Ref. [36]. In the LFE case, a relatively strong constant optical field is added to the diffracted fields off the acoustic gratings before the calculation of the diffraction efficiency, representing the background field present in our experiments.

In Fig. 2 (black dashed curves), we plot the diffracted signals, calculated for the 10 nm Au gratings on 85, 141, and 522 nm thick Au layers measured in both the LFE [Figs. 2(a), 2(c) and 2(e)] and HFE [Figs. 2(b), 2(d) and 2(f)]. Parameters were manually adjusted until the best fit between the measurements and the calculations was obtained and kept constant for both setups.

In Figs. 2(a) and 2(b), the calculations show long-lasting oscillating signals with a period of about 50 ps for the grating fabricated on the 85 nm thick Au layer. The calculations are in good agreement with the experimental results. In the bottom panels of Figs. 2(a) and 2(b), we plot the calculated diffracted signal from only the displacement at the glass–Au interface (blue curve) and from only the strain-optic grating propagating inside the glass (red curve). The latter effect can be viewed as diffraction from spatially periodic changes in the material density induced by the propagating, spatially periodic sound wave. This leads to a spatially periodic, propagating, transient variation of the refractive index of the glass. Such a propagating, spatially periodic refractive index constitutes a grating from which the probe can diffract. The calculated curves clearly show that the signal is dominated by the latter contribution.

In Figs. 2(c) and 2(d) (black dashed curves), we plot the diffracted signals, calculated for the grating on the 141 nm thick Au layer. The calculations also show oscillating signals with a period of approximately 80 ps, in good agreement with the measured signals. There is some mismatch between the measured and calculated diffraction signal strength, especially for longer delays. In the bottom panels of Figs. 2(c) and 2(d), we plot again the calculated diffracted signals from *only* surface displacement (blue curve), and from *only* the strain-optic grating propagating inside the glass (red curve). In contrast to the calculations shown for the 85 nm thick Au layer, here, we find that the displacement of the atoms at the glass–Au interface provides the strongest contribution to the measured signals.

In Figs. 2(e) and 2(f) (black dashed curves), we plot the diffracted signals, calculated for the 522 nm thick Au layer. The calculations show oscillating signals with a period of approximately 285 ps, in good agreement with the measured signals. In the bottom panels of Figs. 2(e) and 2(f), we plot again the calculated diffracted signals from only the acoustic-wave-induced interface grating (blue curve), and from only the strain-optic grating propagating inside the glass (red curve). Note that for this sample, the bigger spacing between the two echoes allows us to identify both contributions in the measurements more easily. The strain-optic contribution appears as a faster oscillating signal superimposed on top of the acoustic-wave-induced interface displacement signal. To simulate the signals measured, a relatively strong constant optical field was added along the first-order diffraction direction, representing the background field present in our experiments. For consistency, the value of the background field was kept the same for the two systems. It has a constant value, corresponding to an intensity on the detector, I_D, which is a fraction of the intensity incident on the sample, I_{INC}. Here, we have $I_D/I_{\mathrm{INC}} = 5 \times 10^{-9}$ for all three samples.

To estimate typical surface displacement amplitudes near the glass–Au interface, we plot in Fig. 5 the calculated displacement of the interface for the 10 nm grating fabricated on a 522 nm thick Au layer, calculated at a pump–probe delay of 285 ps delay, corresponding to the arrival time of the first echo [indicated by the gray dashed line in Figs. 3(a) and 3(b)]. 285 ps is the time at which the diffracted signal due to the displacement is found to be the largest in the calculations. At this time delay, the acoustic wave has completed one round trip inside the 522 nm Au, and the grating-shaped displacement at the glass–Au interface has the same phase as the buried grating. Here, three unit cells are shown, where one unit cell has a width of 6 μm. Fig. 5(a) shows

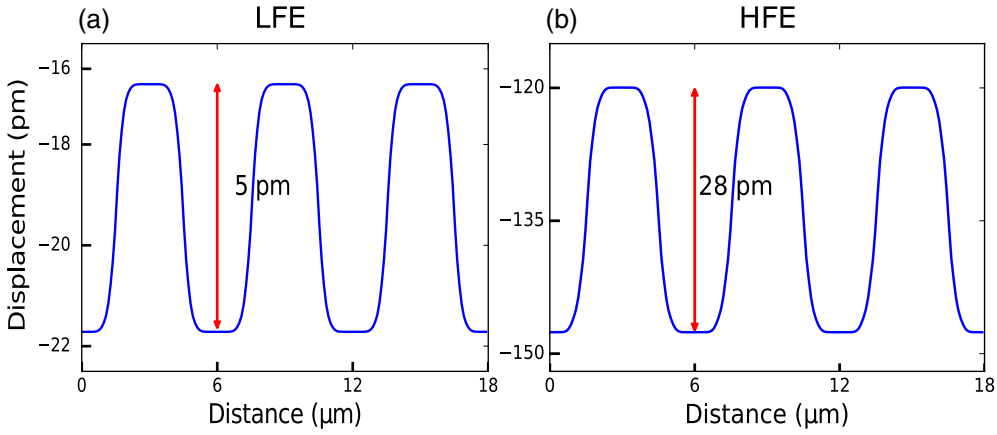

Fig. 5. Displacement at the glass–Au interface for the 522 nm sample, calculated at a delay of 285 ps, as a function of the position along the direction perpendicular to the grating lines in the (a) LFE and (b) HFE.

the interface displacement profile calculated using the LFE parameters and Fig. 5(b) the HFE parameters. In both figures, the displacement profile is superimposed on the expansion of the whole Au layer due to heating, which explains the negative offset in the displacement values. However, only the grating-shaped interface displacement profile contributes to the diffraction efficiency. We obtain a peak-to-valley amplitude of the acoustic-wave-induced interface grating value of 5 pm for the LFE. For the HFE, where the pump fluence is more than five times bigger than the LFE, the peak-to-valley amplitude of the acoustic-wave-induced grating at the glass–Au interface is 28 pm.

5. DISCUSSION

A. Acoustic Wave Generation in Au

Time-resolved measurements of transient reflectivities on thin Au layers as a function of layer thickness have been described before [38,39]. The thickness of the Au layer, however, also plays a role in the acoustic wave generation mechanism. While for the thinner Au layers (85 and 141 nm), the whole layer is rapidly and homogeneously heated up, for the thicker Au layer (522 nm), this is no longer the case. Instead, the acoustic wave generated within a finite depth of about 200–300 nm from the interface will propagate into the material until it reaches the buried grating at the Au–air interface. Here, the acoustic wave is reflected back with a delay between the part reflected off the valleys and the ridges of the grating. As a result, the acoustic wavefront becomes spatially modulated. The arrival time of the first echo corresponds roughly to the round-trip time in the 522 nm thick Au layer. It can be calculated as $T = 2l/v$, where l is the layer thickness, and v is the speed of sound in the metal. Assuming a longitudinal velocity of 3.2 km/s [29], the round-trip time is expected to be ≈303 ps. Finally, once the reflected acoustic wave reaches the glass–Au interface, it displaces the Au atoms in a spatially periodic manner. We can detect this grating by diffraction of a probe pulse.

As we can see from the simulations shown in Fig. 2 (bottom panels) the total diffracted signal predominantly consists of two different contributions. The blue curves represent the diffracted probe beam from the acoustic-wave-induced interface grating at the glass–Au interface. The red curves, instead, represent optical diffraction from the strain-optic wave that has partially entered the glass and continues to propagate [36,37,40–43]. The total oscillatory signal is due to the interference between the different contributions to the diffracted signal. These include, for example, the background optical field, the probe beam diffracting off the strain-optic grating propagating in the glass, and the transmitted probe beam reflecting back at the glass–metal interface and diffracting again from the strain-optic gratings in glass. As was pointed out in Ref. [42], the latter is also often referred to as Brillouin scattering. The period of this oscillation is given by $T = \lambda/(2nv\cos\theta)$ [37]. Here, λ is the probe wavelength, n is the refractive index of the glass at this wavelength, v is the speed of sound in glass, and θ is the angle of incidence, measured inside the glass. For glass, $v \approx 5.7$ km/s, and $n = 1.5$. In our experiments, $\theta = 14.5°$ inside the glass for the LFE and $\theta = 2.0°$ in the HFE. We then obtain an oscillation period of 50.4 ps for the measurements in the LFE and of 46.7 ps for the measurements taken in the HFE. This period is close to the period of the acoustic oscillations for the grating fabricated on 85 nm Au of 50 ± 2 ps for the LFE [see Fig. 2(a)] and of 46 ± 2 ps for the HFE [see Fig. 2(b)]. The contribution from the strain-optic effect in the glass is weaker for the measurements on the 141 nm and 522 nm thick Au layers [see Figs. 2(c)–2(f)]. For the grating fabricated on 522 nm thick Au, the contribution due to the strain-optic effect is a more clearly visible lower amplitude oscillation superimposed on the slower acoustic-wave-induced displacement diffraction peaks [see Figs. 2(e) and 2(f)].

B. "Negative" Diffracted Signals: Background Optical Fields

The clearest difference between measurements taken in the HFE and the LFE is that in the first case, the measured diffracted signal is all positive, while in the latter, it drops below the background level seen at negative delays. This can be explained only if we can assume that *another*, coherent scattered optical field is present, which interferes with the field diffracted by the acoustic wave. Heterodyning of a weak optical field is a widely used technique to improve the sensitivity to small signals. It is achieved by applying on the same photodetector an additional optical field of higher amplitude. The interference between the two fields leads to amplification of the weak field. The source of the second stronger field can be the same laser source [26], a second laser beam [44], or also light scattered from reflecting interfaces of the sample [42,43].

The optical phase difference between the two diffracted fields will determine the extent to which the interference is constructive/destructive. For illustrative purposes only, we will assume that the acoustic wave gives rise to only *one* diffracted field at a time. Denoting the additional background diffracted optical electric field $E_b e^{i(\omega t - \vec{k}\cdot\vec{r})}$, the field diffracted by the acoustic wave $E_{ac} e^{i(\omega t - \vec{k}\cdot\vec{r} + \phi)}$, and the sum of the two fields $E_{\text{tot}} = E_b e^{i(\omega t - \vec{k}\cdot\vec{r})} + E_{ac} e^{i(\omega t - \vec{k}\cdot\vec{r} + \phi)}$, we can write for the total optical power S incident on the Si detector

$$S \propto |E_{\text{tot}}|^2 = E_b^2 + E_{ac}^2 + 2E_b E_{ac}\cos(\phi), \tag{1}$$

where ϕ is a pump–probe delay-dependent difference in phase between the two fields, and where we have suppressed the time dependence of the amplitudes. It is important to realize that in the LFE, the pump pulse train is modulated with a mechanical chopper. Lock-in detection ensures that probe signal components on the detector that are *not* modulated by the pump beam will be removed by the lock-in amplifier. This means that, in principle, only terms containing E_{ac} in Eq. (1) are observed in our measurements. When the background optical field amplitude E_b is constant and has an amplitude much bigger than the field diffracted by the acoustic wave E_{ac} ($E_b \gg E_{ac}$), the E_b^2 term in Eq. (1) serves as a constant background signal level around which the $2E_b E_{ac}\cos(\phi)$ term oscillates when ϕ periodically changes. Lock-in detection ensures that E_b^2 is not observed directly and that when the coherent sum of the two fields drops below the background field strength, this is seen as a negative signal.

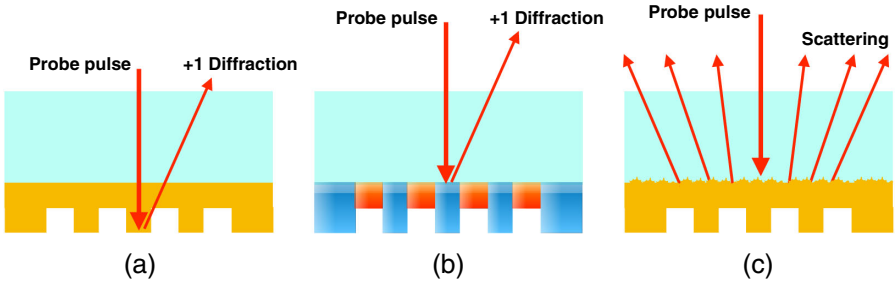

Fig. 6. Schematic representation of the possible sources of background light in our experiments. (a) Direct optical diffraction from the buried grating. (b) Optical diffraction from thermal grating. (c) Scattering by interface roughness.

The above description of the effect of the background optical electric field gives a plausible physical explanation for the observation that the diffracted signals drop below the level seen for negative delays. However, it ignores the fact that, as we explained in Section 5.A, every time the acoustic wave reaches the glass–metal interface, part of the wave is periodically transmitted into the glass where each acoustic wave also gives rise to an additional time-dependent diffraction signal. This means that in reality, the field E_{ac} is composed of several contributions, $E_{ac_k}e^{i\phi_k}$ (k = 1, 2, …), each with a different amplitude E_{ac_k} and a time-dependent phase difference ϕ_k with respect to the background field E_b. Fortunately, using the full numerical model to describe the generation, propagation, and optical detection of the acoustic waves, all these waves are automatically taken into account, as mentioned before.

The optical phase difference between the two diffracted fields will determine whether the interference is constructive or destructive. Destructive interference leads to less light on the detector, which, after lock-in amplification, manifests itself as a negative signal. There are several possible sources of background light in our experiments, which we will discuss next, schematically represented in Fig. 6.

1. Direct Optical Diffraction from the Buried Grating

In principle, for thin layers of Au (thickness <100 nm), probe light could still penetrate the layer and diffract off the buried grating [see Fig. 6(a)]. This diffracted light travels back again through the layer producing a background field on the detector. This may seem surprising in view of the penetration depth of 800 nm light in Au (approx. 13 nm [39]). For such a penetration depth, after traversing the Au layer twice, the signal attenuation would lead to only a weak diffracted signal. For the 141 nm and especially for the 522 nm samples, direct optical diffraction off the buried gratings becomes vanishingly small and is thus unlikely to be the source of the background field. Moreover, direct optical diffraction is unlikely to be the cause of the background field. Figure 3(c) clearly shows the random nature of the sign and amplitude of the diffracted signals when the sample is scanned in the x and y directions. This randomness is caused by a random difference between the phase of light diffracted by the acoustic-wave-induced grating and the background optical field. As the light diffracted directly off the buried grating would always have the same phase as the acoustic-wave-induced interface grating, the optical phase difference between the light diffracted by both gratings would not change.

2. Optical Diffraction from Thermal Grating

When the pump pulse energy is deposited into the material, a thermal grating can be created due to the presence of the buried grating, which gives rise to a periodic variation in Au thickness. As shown in Fig. 6(b), the areas above the valleys of the grating, where the total metal thickness is the lowest, will reach a higher lattice temperature. The areas above the ridges of the grating will have a lower lattice temperature. The initial amplitude of this temperature grating at the interface, ΔT, is thus determined by the difference between the temperatures above the valleys and the ridges of the grating. Heating of the layer leads to changes in the complex dielectric function of the metal. A grating in the temperature thus leads to a grating in the dielectric function. From this grating, a probe pulse can be diffracted. In the LFE, the high repetition rate of the system may lead to a cumulative effect so that when the next probe pulse arrives at the interface, the energy deposited in the metal layer by the previous pump pulse has not yet completely dissipated into the substrate and/or has not been completely washed out by lateral heat diffusion. Thus, a weak quasi-static thermal grating could be present at the interface, which will diffract the probe pulse. However, also diffraction by a thermal grating is unlikely to be the cause of the background field, as a thermal grating would always have the same phase as the acoustic-wave-induced interface grating and would thus not give rise to the strong, random position dependence seen in our measurement. This is supported by our observation that the background field is also clearly present for the gratings on thicker Au layers (522 nm). For this layer, the thickness difference above the valleys and the ridges of the 10 nm amplitude grating becomes relatively small and is thus less likely to lead to a thermal grating. We note that the absence of a thermal grating in our experiments may be a consequence of the modestly high repetition rate of our LFE of 5.1 MHz. Often, mode-locked lasers have a repetition rate of 75 to 100 MHz, which would make thermal gratings more likely, as there is less time for the heat to diffuse into the substrate during the time between two laser pulses.

3. Scattering by Interface Roughness

The sign change of the measured diffracted signals as a function of the position of the probe beam onto the sample (see Section 3)

can be explained only in relation to the nature of the glass–Au interface. The Au layers on which our gratings are fabricated were deposited by thermal evaporation. This technique generates poly-crystalline Au layers with a more or less random distribution of Au crystal sizes and orientations [45]. This means that, as shown in Fig. 4 and discussed in Section 3, the glass–metal interface has a certain roughness of $R_q = 0.60$ nm, which is about two orders of magnitude larger than the amplitude of the acoustic-wave-induced interface grating. Rough surfaces, however, scatter light in all directions [see Fig. 6(c)], whereas a grating, even when its amplitude is considerably smaller than the roughness, diffracts and thus confines light into a few particular diffraction orders only. Nevertheless, a significant background signal was observed in our setup. The light scattered from the surface will have a random phase [46]. Moreover, since roughness has a random character, the scattered light will have a different phase when the interface is illuminated at different positions. This is why our probe beam can detect these phase changes only when the sample is translated over a sufficiently large distance to "see" a statistically different area of the sample. The difference in phase between the two optical fields varies in a random fashion when the beam illuminates different areas, and thus so does the interference between the fields scattered by these two sources.

C. Comparison Between LFE and HFE

Now that we understand why the signals measured in the LFE and the HFE are different, a comparison between the results obtained in the two different setups can be made. We assume the background scattered field amplitude to be time independent in both setups. Suppose that η_s is the efficiency with which the surface roughness scatters the incident probe light onto the detector. The efficiency η_{gr}, with which the acoustic-wave-induced grating diffracts the incident probe light, depends on the square of the amplitude u of the grating, which, in turn, scales linearly with the pump fluence F_{pu}:

$$\eta_{gr} \propto u^2 = C F_{pu}^2, \tag{2}$$

with C a constant of proportionality. The ratio of the two can be written as

$$\frac{\eta_{gr}}{\eta_s} = \frac{C F_{pu}^2}{\eta_s}. \tag{3}$$

Since η_s is independent of the pump fluence, this equation clearly shows that the ratio of the light diffracted by the grating and the light scattered by the surface roughness scales with the square of the pump fluence. Thus, for increasing pump fluence, diffraction by the grating increases relative to scattering by surface roughness.

The difference in the calculated acoustic grating amplitude for the 522 nm sample in the LFE and the HFE (shown in Fig. 5) can be estimated by comparing the fluence of the pump beams for the two different setups. The fluence used for this particular sample is approximately 7 ± 1 J/m^2 in the LFE and 35 ± 3 J/m^2 in the HFE, giving a ratio of about five. The ratio between the amplitudes of the acoustic wave calculated for the HFE and the LFE is ≈5.6, close to the ratio between the two fluences. Taking Eq. (3) into account, the latter number leads to a diffraction efficiency (ignoring the background optical field) of $\eta_{\mathrm{HFE}} \approx 31 \eta_{\mathrm{LFE}}$. Using the expression for the diffraction efficiency of a binary grating [47], we calculate the diffraction efficiencies of acoustic-wave-induced gratings at the interfaces of the three samples used in this work to be on the order of $\approx 10^{-7}$ for the HFE and $\approx 10^{-9}$ for the LFE. Thus, we can conclude that the background signal (surface roughness scattering efficiency of 5×10^{-9}) strongly shapes the measured signals in the LFE, while it can be neglected in the HFE.

In general, it is difficult to predict which system is better for the detection of buried gratings using laser-induced ultrasound. High-fluence, low-repetition-rate lasers are capable of generating strong ultrasound pulses, but have relatively high pulse-to-pulse intensity fluctuations that lead to fluctuating signals and lower detection sensitivity. In addition, high fluences can more easily lead to optical damage when focusing the beam tightly onto the samples, which has to be avoided at all cost. Low-fluence systems have smaller pulse-to-pulse fluctuations, and the pulse train can be modulated, facilitating the use of lock-in detection schemes that enhance detection sensitivity. This may offset signal reduction due to the relatively low peak power of the pulse. However, these arguments assume implicitly that in both cases the detected signals are not significantly affected by the change in repetition rate or fluence, and that changing either has an effect only on signal strength. Our results show that this assumption no longer holds. This is due to the presence of light scattering by interface roughness that scales differently with laser power than the photoacoustic signal.

Despite the fact that in the HFE it is possible to generate stronger acoustic gratings at the glass–metal interface, from an application point of view, the LFE may be a better candidate for the detection of periodic micro-structures buried underneath optically opaque materials. One of the advantages of using the LFE is that, due to the higher repetition rate of the laser, a good signal-to-noise ratio is achievable in less time. In our case, measuring with the LFE allowed us to reduce the acquisition time compared to the HFE. The presence of a strong static background field can attenuate the signal but can also, for the right optical phase difference between the diffracted and scattered fields, amplify the weak acoustic-wave-induced optical signals, making it easier to detect the hidden structures.

6. CONCLUSION

We have shown that different femtosecond laser systems can be used to generate ultrahigh frequency acoustic waves for the detection of periodic micro-structures buried underneath optically opaque layers. In our experiments, diffraction from the "acoustic replica" of the gratings at the glass–metal interface has been measured. We observe that the shapes of the signals measured in the LFE and the HFE are remarkably different, despite the fact that the signals were obtained by measuring on the same sample. This observation can be explained by the presence of a coherent background optical field due to scattering from the interface roughness at the glass–Au interface. In the LFE, this background optical field is significantly stronger than the strength of the optical field diffracted by the acoustic wave. Interference between the two changes the shape of the diffracted

signal as a function of the pump–probe time delay and can cause the signal to drop below the level observed at negative delays when the interference is destructive. In spite of the smaller amplitude of the acoustic grating induced with the LFE, the high repetition rate of the laser system allows us to improve the signal-to-noise ratio, reducing the acquisition time.

Funding. European Research Council ERC-StG, Grant No. (637476); Vrije Universiteit Amsterdam; Universiteit van Amsterdam; ASML; Nederlandse Organisatie voor Wetenschappelijk Onderzoek.

Acknowledgment. S.W. acknowledges funding from the European Research Council (ERC-StG, Grant No. 637476).

Disclosures. The authors declare no conflicts of interest.

REFERENCES

1. A. Nolvi, I. Kassamakov, and E. Hæggström, "Subsurface metrology using scanning white light interferometry: absolute z coordinates deep inside displays," J. Opt. Soc. Am. A **35**, A18–A22 (2018).
2. M. H. van Es, A. Mohtashami, D. Piras, and H. Sadeghian, "Image-based overlay and alignment metrology through optically opaque media with sub-surface probe microscopy," Proc. SPIE **10585**, 105850R (2018).
3. R. van Gastel, G. Hlawacek, H. J. Zandvliet, and B. Poelsema, "Subsurface analysis of semiconductor structures with helium ion microscopy," Microelectron. Reliab. **52**, 2104–2109 (2012).
4. S. Keij, I. Setija, G. van der Zouw, and E. Ebert, "Advances in phase-grating-based wafer alignment systems," Proc. SPIE **5752**, 948–960 (2005).
5. A. J. den Boef, "Optical wafer metrology sensors for process-robust CD and overlay control in semiconductor device manufacturing," Surf. Topogr. **4**, 023001 (2016).
6. O. Matsuda, M. C. Larciprete, R. Li Voti, and O. B. Wright, "Fundamentals of picosecond laser ultrasonics," Ultrasonics **56**, 3–20 (2015).
7. M. Kouyaté, T. Pezeril, V. Gusev, and O. Matsuda, "Theory for optical detection of picosecond shear acoustic gratings," J. Opt. Soc. Am. B **33**, 2634–2648 (2016).
8. P. Ruello and V. E. Gusev, "Physical mechanisms of coherent acoustic phonons generation by ultrafast laser action," Ultrasonics **56**, 21–35 (2015).
9. K. A. Nelson, R. J. D. Miller, D. R. Lutz, and M. D. Fayer, "Optical generation of tunable ultrasonic waves," J. Appl. Phys. **53**, 1144–1149 (1982).
10. C. Thomsen, H. T. Grahn, H. J. Maris, and J. Tauc, "Surface generation and detection of phonons by picosecond light pulses," Phys. Rev. B **34**, 4129–4138 (1986).
11. O. B. Wright and K. Kawashima, "Coherent phonon detection from ultrafast surface vibrations," Phys. Rev. Lett. **69**, 1668–1671 (1992).
12. V. Gusev, "On generation of picosecond inhomogeneous shear strain fronts by laser-induced gratings," Appl. Phys. Lett. **94**, 164105 (2009).
13. O. B. Wright and V. E. Gusev, "Acoustic generation in crystalline silicon with femtosecond optical pulses," Appl. Phys. Lett. **66**, 1190–1192 (1995).
14. H. Maris, "Picosecond ultrasonics," Sci. Am. **278**, 86–89 (1998).
15. T. F. Crimmins, A. A. Maznev, and K. A. Nelson, "Transient grating measurements of picosecond acoustic pulses in metal films," Appl. Phys. Lett. **74**, 1344–1346 (1999).
16. R. M. Slayton and K. A. Nelson, "Picosecond acoustic transmission measurements. Part I. Transient grating generation and detection of acoustic responses in thin metal films," J. Chem. Phys. **120**, 3908–3918 (2004).
17. A. Huynh, N. D. Lanzillotti-Kimura, B. Jusserand, B. Perrin, A. Fainstein, M. F. Pascual-Winter, E. Peronne, and A. Lemaître, "Subterahertz phonon dynamics in acoustic nanocavities," Phys. Rev. Lett. **97**, 115502 (2006).
18. T. Saito, O. Matsuda, and O. B. Wright, "Picosecond acoustic phonon pulse generation in nickel and chromium," Phys. Rev. B **67**, 205421 (2003).
19. F. Pérez-Cota, R. J. Smith, E. Moradi, L. Marques, K. F. Webb, and M. Clark, "High resolution 3D imaging of living cells with sub-optical wavelength phonons," Sci. Rep. **6**, 39326 (2016).
20. B. C. Daly, N. C. R. Holme, T. Buma, C. Branciard, T. B. Norris, D. M. Tennant, J. A. Taylor, J. E. Bower, and S. Pau, "Imaging nanostructures with coherent phonon pulses," Appl. Phys. Lett. **84**, 5180–5182 (2004).
21. T. Saito, O. Matsuda, M. Tomoda, and O. B. Wright, "Imaging gigahertz surface acoustic waves through the photoelastic effect," J. Opt. Soc. Am. B **27**, 2632–2638 (2010).
22. T. W. Murray, M. Haltmeier, T. Berer, E. Leiss-Holzinger, and P. Burgholzer, "Super-resolution photoacoustic microscopy using blind structured illumination," Optica **4**, 17–22 (2017).
23. C. J. K. Richardson, M. J. Ehrlich, and J. W. Wagner, "Interferometric detection of ultrafast thermoelastic transients in thin films: theory with supporting experiment," J. Opt. Soc. Am. B **16**, 1007–1015 (1999).
24. M. Lejman, V. Shalagatskyi, O. Kovalenko, T. Pezeril, V. V. Temnov, and P. Ruello, "Ultrafast optical detection of coherent acoustic phonons emission driven by superdiffusive hot electrons," J. Opt. Soc. Am. B **31**, 282–290 (2014).
25. Z. Ge, D. G. Cahill, and P. V. Braun, "AuPd metal nanoparticles as probes of nanoscale thermal transport in aqueous solution," J. Phys. Chem. B **108**, 18870–18875 (2004).
26. A. A. Maznev, K. A. Nelson, and J. A. Rogers, "Optical heterodyne detection of laser-induced gratings," Opt. Lett. **23**, 1319–1321 (1998).
27. C. Grünsteidl, T. Berer, M. Hettich, and I. Veres, "Using zero-group-velocity lamb waves to determine thickness and bulk sound velocities of isotropic plates," AIP Conf. Proc. **2102**, 050016 (2019).
28. B. Bonello, B. Perrin, E. Romatet, and J. Jeannet, "Application of the picosecond ultrasonic technique to the study of elastic and time-resolved thermal properties of materials," Ultrasonics **35**, 223–231 (1997).
29. O. B. Wright, "Ultrafast nonequilibrium stress generation in gold and silver," Phys. Rev. B **49**, 9985–9988 (1994).
30. D. Yarotski, E. Fu, L. Yan, Q. Jia, Y. Wang, A. J. Taylor, and B. P. Uberuaga, "Characterization of irradiation damage distribution near $TiO_2/SrTiO_3$ interfaces using coherent acoustic phonon interferometry," Appl. Phys. Lett. **100**, 251603 (2012).
31. S. Edward, H. Zhang, I. Setija, V. Verrina, A. Antoncecchi, S. Witte, and P. Planken, "Detection of hidden gratings through multilayer nanostructures using light and sound," Phys. Rev. Appl. **14**, 014015 (2020).
32. S. Edward, A. Antoncecchi, H. Zhang, H. Sielcken, S. Witte, and P. C. M. Planken, "Detection of periodic structures through opaque metal layers by optical measurements of ultrafast electron dynamics," Opt. Express **26**, 23380–23396 (2018).
33. X. Yu, Y. Shi, T. Wang, and X. Sun, "Dust-concentration measurement based on Mie scattering of a laser beam," PLoS ONE **12**, 1–15 (2017).
34. S. Schröder, A. Duparré, L. Coriand, A. Tünnermann, D. H. Penalver, and J. E. Harvey, "Modeling of light scattering in different regimes of surface roughness," Opt. Express **19**, 9820–9835 (2011).
35. P. Benjamin and C. Weaver, "The adhesion of evaporated metal films on glass," Proc. R. Soc. London Ser. A **261**, 516–531 (1961).
36. H. Zhang, A. Antoncecchi, S. Edward, I. Setija, P. Planken, and S. Witte, "Unraveling phononic, optoacoustic, and mechanical properties of metals with light-driven hypersound," Phys. Rev. Appl. **13**, 014010 (2020).
37. A. Devos, R. Côte, G. Caruyer, and A. Lefèvre, "A different way of performing picosecond ultrasonic measurements in thin transparent films based on laser-wavelength effects," Appl. Phys. Lett. **86**, 211903 (2005).

38. J. Hohlfeld, J. Müller, S.-S. Wellershoff, and E. Matthias, "Time-resolved thermoreflectivity of thin gold films and its dependence on film thickness," Appl. Phys. B **64**, 387–390 (1997).
39. J. Hohlfeld, S.-S. Wellershoff, J. Güdde, U. Conrad, V. Jähnke, and E. Matthias, "Electron and lattice dynamics following optical excitation of metals," Chem. Phys. **251**, 237–258 (2000).
40. H. N. Lin, R. J. Stoner, H. J. Maris, and J. Tauc, "Phonon attenuation and velocity measurements in transparent materials by picosecond acoustic interferometry," J. Appl. Phys. **69**, 3816–3822 (1991).
41. H. Lin, H. J. Maris, L. B. Freund, K. Y. Lee, H. Luhn, and D. P. Kern, "Study of vibrational modes of gold nanostructures by picosecond ultrasonics," J. Appl. Phys. **73**, 37–45 (1993).
42. O. Matsuda, T. Pezeril, I. Chaban, K. Fujita, and V. Gusev, "Time-domain Brillouin scattering assisted by diffraction gratings," Phys. Rev. B **97**, 064301 (2018).
43. V. E. Gusev and P. Ruello, "Advances in applications of time-domain Brillouin scattering for nanoscale imaging," Appl. Phys. Rev. **5**, 031101 (2018).
44. G. G. Kozlov, V. S. Zapasskii, and P. Y. Shapochkin, "Heterodyne detection of scattered light: application to mapping and tomography of optically inhomogeneous media," Appl. Opt. **57**, B170–B178 (2018).
45. P. Barna and G. Radnóczi, "Structure formation during deposition of polycrystalline metallic thin films," in *Metallic Films for Electronic, Optical and Magnetic Applications*, K. Barmak and K. Coffey, eds. (Woodhead Publishing, 2014), pp. 67–120.
46. J. A. DeSanto, *Overview of Rough Surface Scattering* (Springer, 2007).
47. Y.-C. Chang, P. Zhou, and J. H. Burge, "Analysis of phase sensitivity for binary computer-generated holograms," Appl. Opt. **45**, 4223–4234 (2006).